

3D printed concrete walls reinforced with flexible FRP textile: Automatic construction, digital rebuilding, and seismic performance

Daobo Zhang^a, Peng Feng^{a,*}, Peizhao Zhou^a, Weiguo Xu^b, Guowei Ma^c

^a Department of Civil Engineering, Tsinghua University, Beijing, China

^b School of Architecture, Tsinghua University, Beijing, China

^c School of Civil and Transportation Engineering, Hebei University of Technology, Tianjin, China

ARTICLE INFO

Keywords:

3D concrete printed wall
BEH loop
Flexible FRP textile
Digital rebuilding
Seismic performance

ABSTRACT

As numerous impressive large-scale 3D printed concrete structures have been built with 3D concrete printing (3DCP) technology, more attention has been given to the automation, accuracy and reliability of this technology. The concept of Brain-Eyes-Hands Loop (BEH Loop) is defined for use in automatic construction, describing the relationships among design, evaluation, and construction. In this paper, an innovative continuous reinforcement method with fiber reinforced polymer (FRP) flexible textile and Engineered Cementitious Composite (ECC) is presented, that offers an effective solution for the lack of tensile reinforcement and corrosion of steel bars in 3D printed concrete structures. The reinforced 3D printed concrete walls were constructed, evaluated, and tested under quasi-static cyclic loading. By digital rebuilding and geometric evaluation, the printing quality of wall specimens was accessed and ensured. Based on the mechanical tests, the seismic performances of the wall specimens were obtained and found to be mainly bending failure. The proposed reinforcement method was demonstrated for delaying crushing and improving mechanical behaviors. The end column and smaller height-width ratio also showed much improvement in mechanical performance. Compared with the conventional cast concrete wall, the 3DCP wall specimens reinforced by the proposed reinforcement method showed better material utilization efficiency and mechanical properties. Therefore, the 3DCP structures reinforced with flexible FRP textile show great potential for the future use in fully automatic construction of large-scale complex architectures according to the frame of the BEH Loop.

1. Introduction

With the development of automatic construction technology and additive manufacturing technology in recent decades, a considerable number of creative architecture projects have been completed [1–6]. 3D concrete printing (3DCP) technology, one of the most promising technologies, provides many new possibilities for making complex curved structures because of its excellent efficiency [7–11] and precision [12–17], low cost [18–22] and potential low environmental impacts [23–26]. With plans for more demonstration projects, 3DCP technology must still address many key challenges, such as reinforcement methods, geometric evaluations and mechanical performances. A systemic methodology of automatic construction for the 3DCP building must be discussed in detail.

Considering the weak tensile, shear, and flexural capabilities of concrete, 3DCP technology is limited in engineering applications due to

the lack of proper reinforcement methods, which arouses much interest from researchers. As a compromised method, 3D concrete printed formworks for conventional casting have been widely implemented, especially in large-scale structures, by Wang Li [27], China Construction Second Engineering Bureau LTD [28], Winsun [29], ETH [12], Apis Cor [30], and so on. Post-tension in 3D concrete printed structures based on traditional construction technologies is another feasible method [20,31–34]. Flexible cables embedded in the concrete filament have also been verified as an efficient method [35–37]. Some researchers proposed and tested an interlayer reinforcement method by inserting steel nails, steel bars, or barbed wires during the printing process [38–42]. However, almost all the reinforcement mentioned above use the steel material, which is vulnerable to corrosion in service due to the interfacial gaps between 3D printed concrete filaments and insufficient concrete cover. Moreover, these reinforcement methods are more suitable for regular rather than complex structures because complex shapes may

* Corresponding author.

E-mail addresses: fengpeng@tsinghua.edu.cn (P. Feng), xwg@tsinghua.edu.cn (W. Xu), guowei.ma@hebut.edu.cn (G. Ma).

necessitate extra construction procedures. It is difficult to use some of these methods in fully digitalized automatic construction by robotic arms because of their needs for operator decisions and manual operations. Therefore, more novel automatic reinforcement methods with advanced materials for 3DCP structures need to be explored.

Another challenge of 3DCP structures is irregular surfaces commonly caused by the periodic layers and the deformation under self-weight. Hence, the monitoring, evaluation, and digitalization of printing qualities and geometric models for 3D concrete printed structures have recently attracted more attention from researchers. Ketel et al. [43] used laser triangulation-based 3D scanning to assess the external geometrics of 3D printed components. A printability index defined from the scanned point cloud was presented and used for the assessment and quality control of 3D printed components. Wolfs et al. [44] used a non-contacting optic measurement system to compute the failure-deformation mode of 3DCP cylinders during printing. The 3D coordinates of the surface points were accessed by high-resolution photographs in real time. Anton et al. [12] scanned twelve 3DCP columns and generated 3D deviation maps from the acquired point clouds based on CAD models. Some cross sections at selected regions indicated that curved parts may have induced larger deviations. Buswell et al. [16] proposed a systematic method to evaluate and assure the geometric quality of parts in 3DCP systems. Three categories of digital measurements, linear dimensions, surface flatness, and feature replication, were used in a 3D printed benchmark, and then the milled application was subtracted. The measurements and analysis focused on the macroscopic dimensions and geometric characteristics, such as the length, width, and height of the walls. Xu et al. [45] proposed a thorough approach based on a geometric dimensioning and tolerancing framework for quantifying 3DCP process capability. Two geometric characteristics, namely the flatness and the profile, were selected for evaluating nine 3DCP parts. Nair et al. [46] proposed a printability accuracy index based on centroidal distances as a global quantifier of print quality. A cylindrical printed concrete specimen was used for scaled-up scanning validation. However, most studies focused on accessing and evaluating macroscopic 3D geometric deviations between scanned models and design models. It is necessary to further rebuild and utilize scanned models of large-scale 3DCP structures, especially during the design stage of automatic construction.

Furthermore, the safety and reliability of service stages are always concerns for large-scale 3DCP structures, which mostly depend on their mechanical performances [47]. However, thus far, most researchers have focused on tests of concrete materials, and only a few mechanical experiments with large-scale 3DCP structures have been conducted [48]. As the main vertical structural component, walls deserve to be studied thoroughly in terms of their mechanical performance since they easily can be automatically constructed on site. Some researchers have recently performed simple loading tests of 3DCP walls, as shown in Table 1. Only simple axial compressive or eccentric compression loading was conducted for full-size 3DCP walls, and the failure modes and mechanical performance were determined. To the best of our knowledge,

there are no references about complicated loading conditions of large-scale 3DCP walls in the literature. Similar to the traditional reinforcement method, steel bars were mostly used in these printing processes, which means that it is necessary to stop the printing process, and the corrosion problem is still present. Unfortunately, most of those studies found that the reinforcing method had a weakening effect on the integrity of wall specimens. In summary, considering that practical large-scale 3DCP walls must face multiloading conditions, for example, seismic conditions, their mechanical performance under those complex loading conditions should be further studied along with new reinforcement methods.

Thus, in this study, the concept of Brain-Eyes-Hands Loop (BEH Loop) was defined and applied to automatic construction. Correspondingly, an innovative automatic continuous reinforcement method with a fiber-reinforced polymer flexible textile and ECC for 3DCP structures was developed. Furthermore, complicated quasi-static cyclic loading conditions of three large-scale 3D printed concrete walls and a cast concrete wall were conducted to determine the seismic performance. Before reinforcing and testing, the printed walls were fully scanned, and then the accurate models were rebuilt, contributing to the locations of the automation construction stage serving as eyes. Through mechanical tests of the walls, the effects of edge columns, height-width ratio, and construction method on the failure mode, load capacity, energy dissipation, and stiffness of walls were investigated and analyzed. Moreover, mass normalized characteristics were discussed in the context of the demand for enhancing material efficiency and reducing carbon emissions.

2. Automatic construction

With the increasingly urgent demand for construction industrialization, intelligent construction and extreme environment construction, the rapid and unmanned automatic construction technology has become the development trend of civil engineering. Thus, an innovative BEH Loop is proposed and illustrated for future automatic construction in Fig. 1. In the BEH Loop, three key symbolization elements, namely the brain, eyes and hands, are introduced, which refer separately to the design, measurement and construction stages. The brain is responsible for structural design based on architectural aesthetics, mechanical analysis, and topology optimization. The eyes can access geometric information of structures by automatic scanning robots and then digitally rebuild an accurate real model. The hands will realize the automatic printing and reinforcement of structures by the robot arms. The brain, eyes, and hands are connected and influenced by each other, thus composing the BEH loop. Specifically, the brain needs the hands to complete the designed structures based on the information that the eyes access. Following the location by the eyes, the hands can print and reinforce structures more precisely. Meanwhile, the eyes can verify the design through digital rebuilding and geometric evaluation. In brief, the proposed BEH Loop clearly illustrates the concept, the procedure, and the relationships of automatically constructing 3DCP structures in the

Table 1
Overview of 3DCP walls under mechanical loading conditions in the literature.

References	Year	Object	Scale (H: height, W: width T: thickness)	Reinforcement	Loading condition
Han et al.[49]	2022	Eight walls with different height to thickness	H (720–2400) mm * W 710 mm * T 240 mm	Six walls with horizontal steel reinforcement, two walls without	Axial compression
Zhang et al.[50]	2022	Twelve core-column walls	H 1200 mm * W 1040 mm * T 240 mm	The core columns with stirrup and transverse steel reinforcement	Axial compression
Daungwilailuk et al. [51]	2021	Two patterns of walls	H 970 mm * W 1320 mm * T 120 mm	Without extra reinforcement	Axial compression
Zhang et al.[52]	2021	Eight walls with different section forms and material strengths	H 800 mm * W 800 mm * T 160 mm	Vertical steel bars and transverse steel frames	Axial compression
Cai et al.[53]	2021	Ten walls with different section forms and eccentricity	H 800 mm * W (800–1000) mm * T 160 mm	Vertical steel bars and transverse steel frames	Eccentric compression

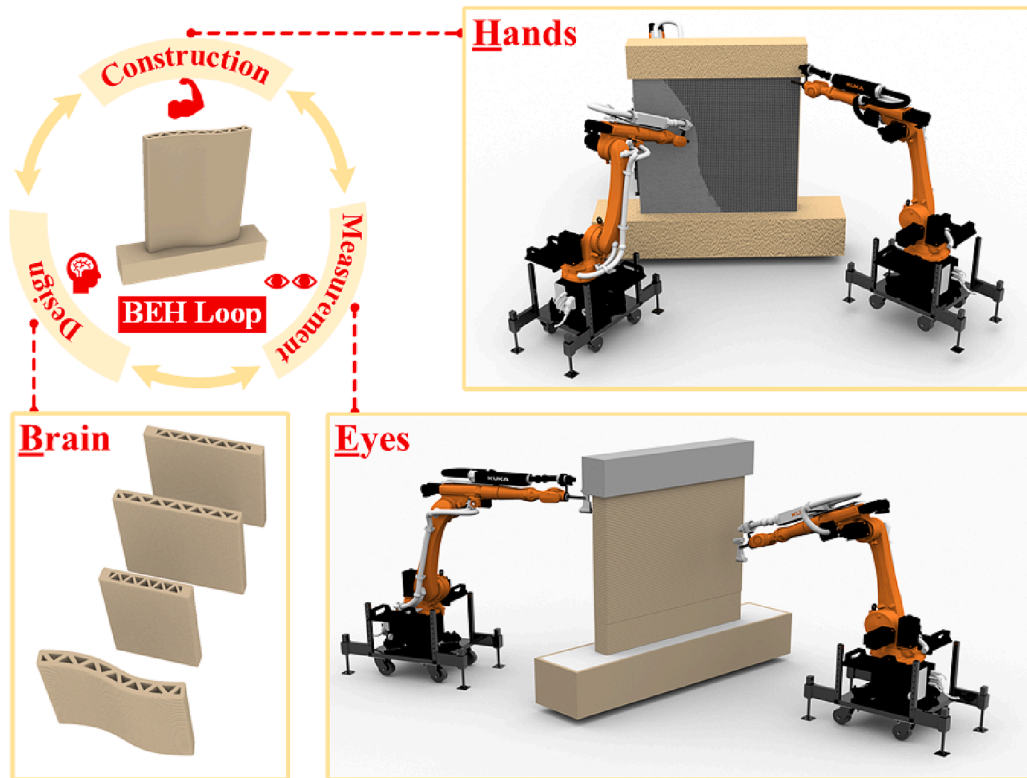


Fig. 1. The proposed BEH Loop is composed of the brain, eyes, and hands.

future. With the BEH Loop, rapid, unmanned and low-cost construction can be achieved with robots. Moreover, buildings and infrastructures can be created in remote and challenging regions of the Earth and the space, such as deep ground, deep sea, polar region and the moon. However, as a necessary key to the hands of the BEH Loop, an automatic and effective reinforcement method is urgently needed.

Therefore, a 3DCP structure reinforced with flexible FRP textile and ECC is proposed, as shown in Fig. 2. With the advantages of automatic construction, light weight and high strength, corrosion resistance and flexibility, the reinforcement method can support the automatic construction of the BEH Loop for remarkable and reliable buildings.

The automatic reinforcement process is as follows. After the concrete structures are first designed and printed by 3D concrete printing robots, they are scanned and evaluated carefully. With the help of location and identification of digitalized scanned models already rebuilt, the outsides of the aim structures are sprayed with an ECC layer (approximately 5 mm thick) by the automatic shotcrete robot, and then several layers of flexible FRP textile are automatically stuck upon the ECC layer by the FRP textile fixing robot. Finally, another ECC layer (approximately 0.5 mm thickness) is automatically resprayed. Overall, automatic

construction combining 3D printing technology and the automatic reinforcement method with flexible FRP textile can realize the full automation of large-scale 3DCP structures with the help of robotic arms.

In the proposed reinforcement method, FRP has great advantages in improving and reinforcing the mechanical properties of structures due to its high strength, low weight, convenient construction and freeform characteristics [54–56]. Moreover, flexible FRP textile-reinforced ECC material is widely adopted to strengthen traditional structural elements such as reinforced concrete (RC) slabs [57,58], beams [59–61] and columns [62,63] for the capacities of reinforcing the confinement stiffness, distributing local stress and controlling material cracks [64–68]. Specifically, the designable flexible FRP textile and ECC material mainly provide tensile and bending capacity, and the inner 3D printed concrete can provide compressive capacity, as shown in Fig. 2a. The irregular surfaces of 3DCP structures are especially helpful for the integration and connectivity between the lightweight outer reinforcing layers and the inner 3DP concrete. Different components can be further integrated by the reinforcement method after assembly owing to its light weight and convenience.

Furthermore, there is no longer electrochemical corrosion problem

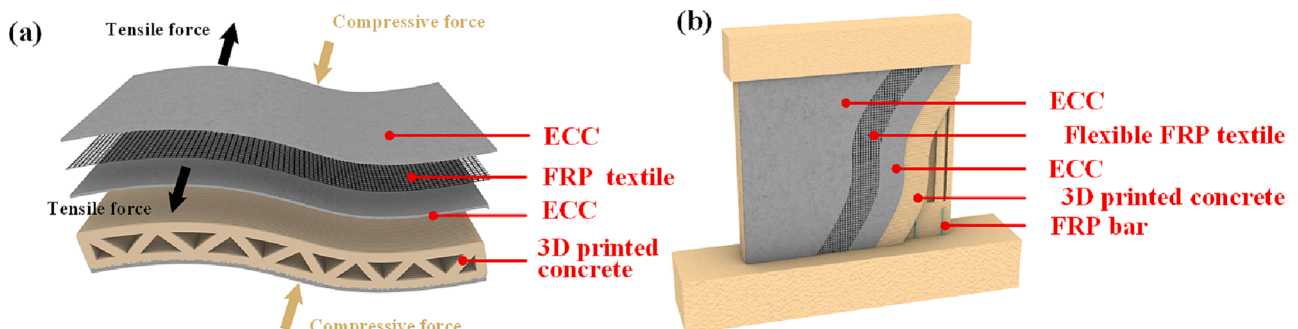


Fig. 2. The proposed reinforcement method. (a), Schematic illustration of the structure. (b), Schematic illustration of the tested wall specimen.

because steel material is not utilized in this reinforcement method. Due to the good durability of FRP and ECC materials, the 3DCP structures reinforced with the proposed method can meet the durability requirement of building structures.

Moreover, the proposed reinforcement method is perfectly compatible with complex curved surfaces, which can realize more designability and possibility for large-scale 3D printed nonlinear buildings. Compared with existing reinforcement methods, the proposed reinforcement method will not destroy the continuity of the printing process for 3D

printed nonlinear buildings. With no extra process introduced during printing, the flexibility and feasibility of flexible FRP textiles are fully utilized. Additionally, the irregular surfaces of 3D printed structures have already been smoothed simultaneously.

In brief, with the automatic construction process, light weight, no corrosion, and more flexible freedom, the proposed reinforcement method can play an important role in the automatic construction of the BEH Loop.

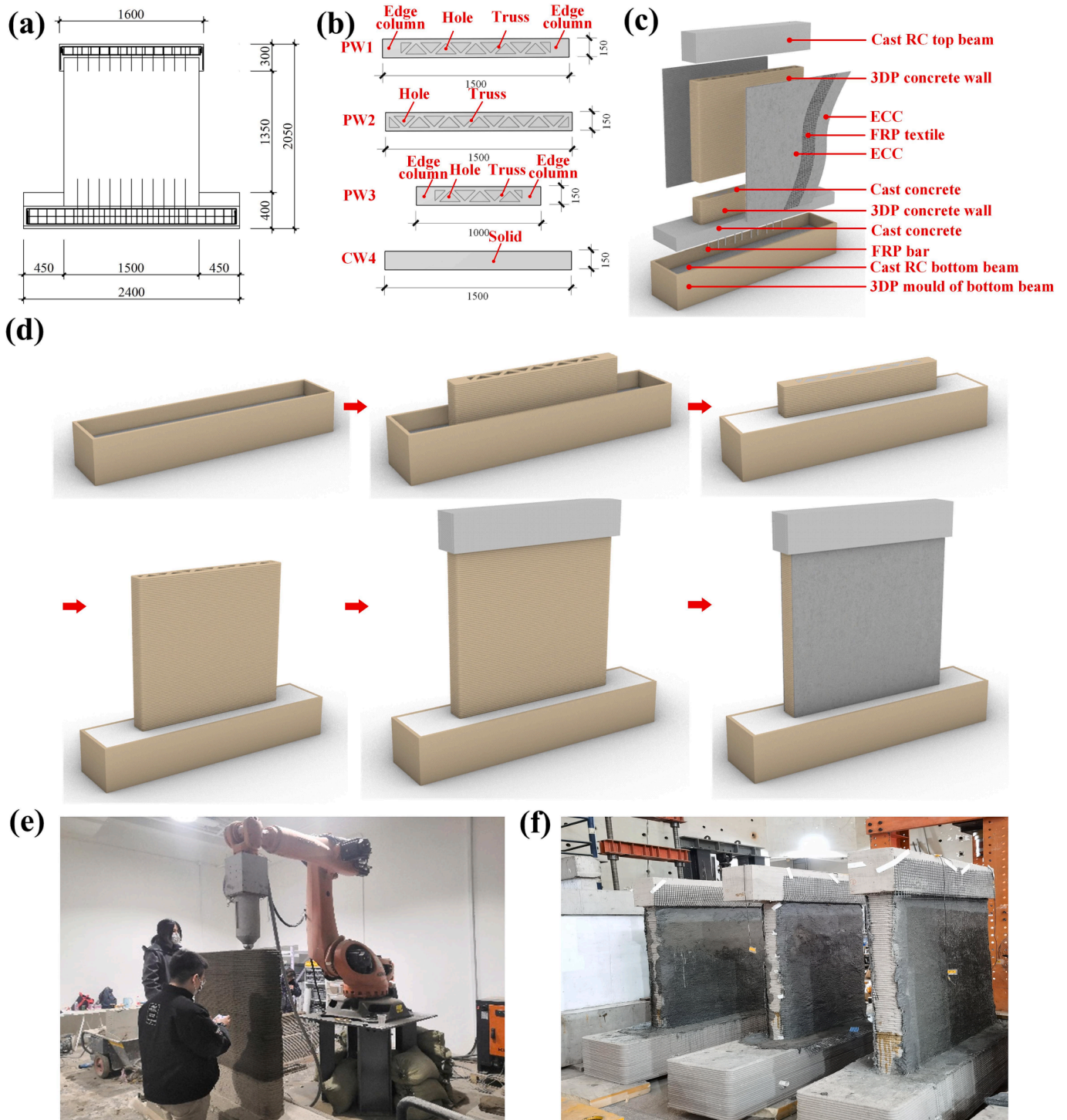


Fig. 3. Details of the wall specimens. (a), Elevation drawing of specimen PW1. (b), Cross sections of the wall specimens. (c), Schematic structure of the wall specimen. (d), Schematic illustration of the construction process. (e), The printing process of the walls by the robotic arm system. (f), Tested walls after reinforcement.

3. Experimental program

3.1. Printing and reinforcement

To demonstrate the BEH Loop with the reinforcement method, three 3D printed concrete walls and one cast concrete wall were designed, optimized, and manufactured based on masonry wall concept. They were conducted to seek for the possibility of replacing traditional masonry walls. The three concrete printed walls were printed by a robotic arm system in the laboratory and then reinforced on site following the proposed reinforcement method with flexible carbon fiber reinforced polymer (CFRP) textile and ECC material. The reinforcing process was conducted manually limited by the robot machines. All four specimens had a height of 1500 mm and a height-width ratio of 1.0 or 1.5 (Fig. 3a). From the cross sections of the specimens shown in Fig. 3b, specimens PW1, PW2 and PW3 were printed with trusses and holes, while specimen CW4 was ordinary cast solidly in the main part. Masonry walls were not chosen as the control specimens for the potential influence and complex interface of different brick and mortar materials. Therefore, the specimen CW4 without reinforcement was cast with concrete to simulate traditional masonry walls without reinforcement. Among the specimens, only specimens PW1 and PW3 had edge columns as boundary elements. The width of the outline in the 3D printed wall specimens was controlled to 30 mm, which was only one concrete filament. All the main bodies of the specimens shared the same concrete materials. To keep the wall fixed and apply the lateral load, a top beam with a cross-section of 250 mm × 300 mm and a foundation beam with a cross-section of 400 mm × 500 mm were cast together with the main body of the wall. Additionally, short glass fiber reinforced polymer (GFRP) bars (250 mm and 570 mm in length) were embedded to ensure a good connection with the top beam and bottom beam separately in all the wall specimens, resulting in the solid parts of the 3D printed walls being 270 mm above the bottom beam. Fig. 3c illustrates the schematic structure of the tested walls. Each hole of the 3D printed walls was inserted with one GFRP bar manually, and there were no GFRP bars in the edge column part so that the disturbance of the 3D printing process was avoided. Moreover, the detailed schematic construction process is shown in Fig. 3d. First, the mold of the bottom beams and then the solid parts of the walls were printed. Corresponding inner hole spaces were cast with concrete after inserting bars. After the main parts of the walls had been printed, the top beams were cast. Finally, the construction processes of reinforcement were finished. The thickness of each reinforcement layer including the ECC layers and the CFRP textile layer were approximately 5 mm totally. The designed section of the 3D printed concrete filament was 30 mm (width) × 15 mm (height). The printing process and final tested walls can be observed in Fig. 3e and Fig. 3f.

Table 2 shows the details of all the specimens. For the loading tests, the constant axial force applied to the wall specimens was determined according to Eq. (1).

Table 2
Specimen details.

Specimen	Manufacture	Height × Width × Thickness (mm)	Edge column (mm)	Height-width ratio	Average section area (mm ²)	Mass (kg)	Axial force (kN)	Design axial force ratio	Real axial force ratio (%)
PW1	3D printed	1500 × 1500 × 150	150 × 150	1.0	154,798	549.5	354.8	0.15	0.07
PW2	3D printed	1500 × 1000 × 150	/	1.0	140,757	517.7	322.6	0.15	0.07
PW3	3D printed	1500 × 1500 × 150	150 × 150	1.5	109,354	446.5	250.6	0.15	0.07
CW4	Cast with mold	1500 × 1500 × 150	/	1.0	225,000	708.8	515.6	0.15	0.07

$$\mu = \frac{N}{f_c A} \quad (1)$$

where N is the design axial force, which was 1.2 times the test values of the axial force applied on the wall specimen [6,69,70]; f_c is the design compressive strength of the concrete; and A represents the average sectional area of the wall specimens. The design axial force ratios μ for all specimens were 0.15 in the tests. Considering 3D printing building are all low-rise buildings for now, the low axial force ratios were selected.

3.2. Material properties

The compositions of the 3D printing concrete and ECC material are shown separately in Table 3 and Table 4. The concrete materials developed in this study can meet the requirements of printability and constructability. Polypropylene (PP) fibers were added to sulfoaluminate cement-based 3D printing concrete to enhance the printing and mechanical properties. The concrete strength of the 3D printing concrete was grade C40, while the tested average compressive strength (150 mm cast cubes) was 45.0 MPa at 28 days. The strengths of the 150 mm 3D printed cubes in different directions were similar to those of the cast cubes (44.96 MPa in the X-direction and 45.59 MPa in the Z-direction). More detailed mechanical properties can be found in Table 5. The failures of tested wall specimens were ensured in the interfaces of layers during the splitting tensile test, the flexural test, and the tensile test. For the Portland cement-based ECC, polyvinyl alcohol (PVA) fibers with 2% fiber volume fraction were added. The measured cubic strength (150 mm cast cubes) of ECC in compressive loading tests was 59.2 MPa at 28 days. Table 6 and Table 7 show the information and properties of the flexible CFRP textile and GFRP bar applied in the specimens, respectively. The elastic modulus, tensile strength, and ultimate strain of a single yarn for the CFRP textile are 211 GPa, 2300 MPa, and 1.09%, respectively.

4. Digital rebuilding

4.1. Scan methodology

To obtain the real scanned model and evaluate the geometric accuracy of 3D printed wall specimens before reinforcement, 3D laser scanning technology was adopted. Considering the scale of the walls, a time-of-flight handheld scanner was introduced, as shown in Fig. 4a. The detailed product specifications can be obtained in [71]. The scanner was only 0.8 kg and approximately 130 × 80 × 300 mm, convenient for operation by hands or robot arms. In addition, the scanner had a measurement range up to 6 m and range accuracy of 0.3 mm, which met the requirement for geometric evaluation. Moreover, the scanner has already been implemented and verified for successfully evaluating the

Table 3
Composition of 3D printing concrete.

Composition	Sulphoaluminate cement	Sand	Water	Superplasticizer	Admixtures	Polypropylene fiber (9 mm)
Mass(%)	42.02	46.22	10.50	0.42	0.42	0.42

Table 4
Composition of ECC.

Composition	Portland cement	fly ash	Sand	Water	Superplasticizer
Mass(%)	27.98	33.58	22.10	16.00	0.34

Table 5
Mechanical properties of 3D printing concrete.

Compressive strength (MPa)	Splitting tensile strength (MPa)	Flexural strength (MPa)	Tensile strength (MPa)	Elastic modulus (GPa)
45.0	2.5	3.4	1.5	18.9

geometric imperfections of building components [71].

Considering the size of the wall specimens and the accuracy of the scan, the scan plan of multiple scanning stages was conducted. The scan of each wall specimen was divided into four or five stages. Then, all the point clouds obtained in each stage were assembled via the commercial software Geomagic Control according to the overlapped regions. The on-site scanning process is shown in Fig. 4b. Reflective markers were first sprayed and well distributed on the surface of the wall specimens to locate the spatial coordinates of the characteristic surface. Before each scan stage, the scanner was calibrated through a calibration board to ensure scanning accuracy. A laptop was used to show the real-time display figure of point clouds during scanning. Furthermore, an auto-scanning robot was designed to achieve fully automatic scanning, as illustrated in Fig. 1. Robotic arms carrying scanners with mobile bases were used to achieve the full-auto scanning process and replace hand-held scanning for now.

4.2. Digital procedure

Based on the point cloud data of wall specimens, complete scanning models were established to reflect the true surfaces of walls. To better evaluate and compare the geometric deviations between 3D printed specimens and designed specimens, a digital procedure of scanning models was developed that was suitable for 3D printed structures. Correspondingly, digital accurate models were rebuilt to fulfill the demand for simulating accurate geometric characteristics for designers. With the scanning models and accurate models digitally rebuilt, robots could realize automatic construction, while the real-time construction situation and deviations were remotely available and accessible to designers.

Taking the wall specimens as an example, the digital procedure was composed of five stages, as follows.

(1) Generation of scanning models. The cloud point pieces of each wall were assembled via Geomagic Control according to the automatic minimum variance method and then manually adjusted by key shape characteristics. Furthermore, over 10 million points for each wall specimen were left after carefully removing the noise points.

Table 6
Properties of flexible CFRP textile.

Textile	Producer	Type of yarn	Grid space (mm)	Mass (g/cm ³)	Cross section of each yarn (mm ²)	Width of mesh (mm)	Width of single rib (mm)
Carbon	CARBON	12KT700 × 2	20 × 20	160	0.85	20 ± 5	3 ± 1

Additionally, the obtained point clouds were wrapped into triangles, thus forming the surfaces of the wall specimens. The rough outside surfaces of 3D printed concrete filaments in wall specimens had already been thoroughly captured, as shown in Fig. 4c.

(2) Extraction of key sections. 3D printed concrete structures, especially those with complex surfaces and irregular characteristics, usually share complex spatial printing paths, sometimes even with changeable heights of printing filaments in the Z direction. Therefore, the regular 2D model data were extracted from the key structural sections that were sliced from 3D scanning models. These 2D model data contributed to rebuilding accurate models based on the layer-by-layer printing mechanism. Because of the constant printing filament size of each wall specimen, ten sliced key sections were conducted, as illustrated in Fig. 4d.

(3) Digitalization of key sections. The geometric key sections were converted into digital models for further analysis and evaluations. The digitalization of filament shapes from key sections was realized by the 3D drawing software Rhino and Grasshopper. The battery module is shown in Fig. 4e. The refined coordinates and key parameters of the wall surfaces were measured and collected.

(4) Simulation of filament shape. Based on the unique filament characteristics of 3D printed structures, the periodic curves were picked and optimized to fit and simulate the surface topography. Thus, the average surface shapes of printing filaments in 3D printed structures were determined.

(5) Rebuilding of accurate models. Based on the obtained average filament shapes and printing path, the assembly and reconstruction of accurate fitting models with complex surfaces were generated and rebuilt to replace the traditional design model with a smooth surface. The accurate models of the wall specimens were rebuilt and are shown in Fig. 4f.

Through the digital procedure, accurate models of wall specimens were rebuilt. Compared with the design models, the accurate wall models could illustrate the unique surfaces of 3DCP walls and were more similar to the real wall specimens. The details of the wall specimens remained to some extent, and unnecessary random data were simplified. Based on the digitally rebuilt accurate models, further geometric evaluations could be studied by designers.

4.3. Geometric evaluation

Fig. 5 illustrates the results of geometric deviations and printing evaluations of the wall specimens based on digital rebuilding. As shown in Fig. 5a, the deviations at the bottom of the wall specimens were larger

Table 7
Mechanical properties of the GFRP bar.

Diameter (mm)	Section area (mm ²)	Ultimate tensile strength (MPa)	Elastic modulus (GPa)	Ultimate tensile strain (%)
12.2	101	1029	43	2.39

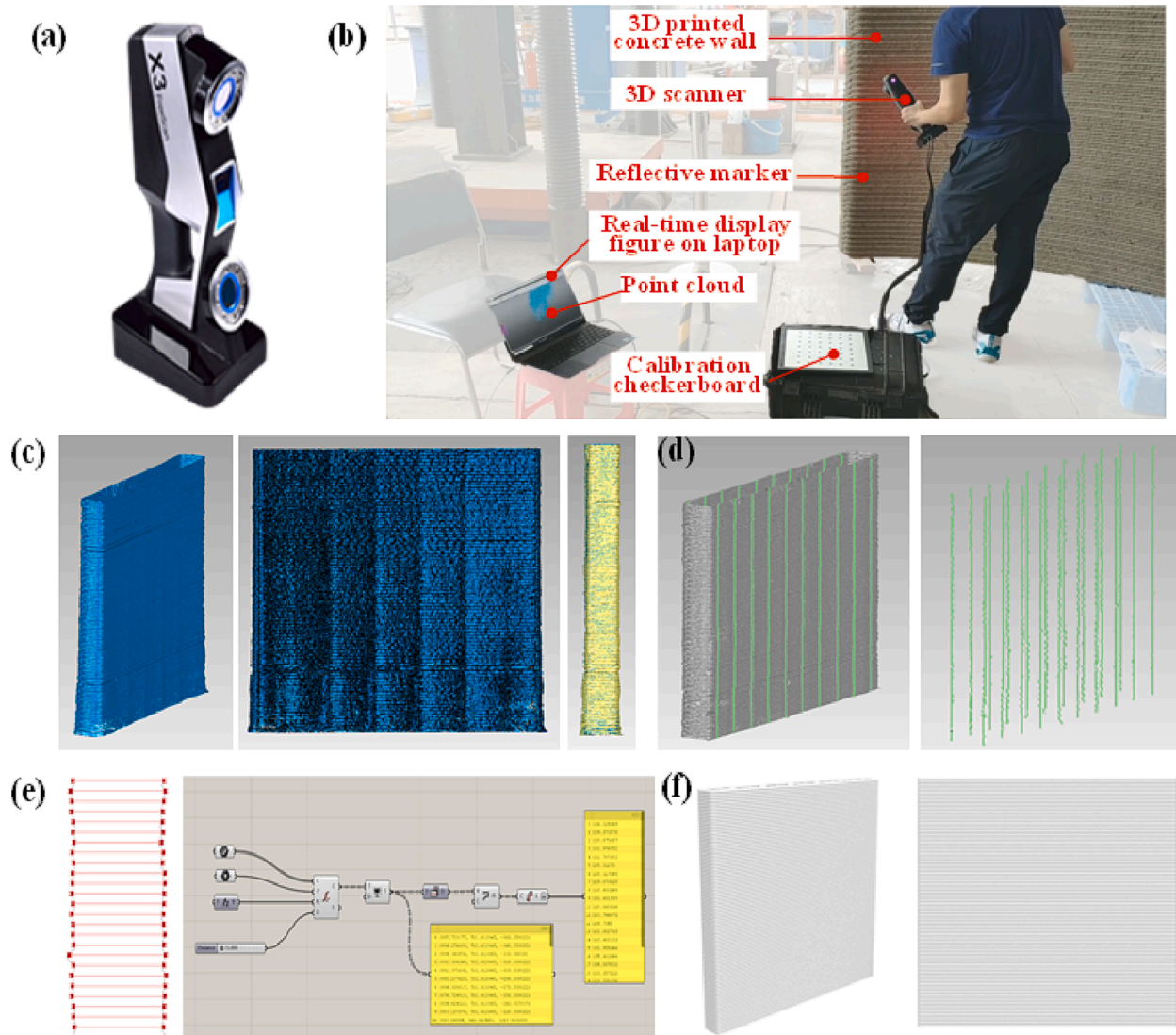


Fig. 4. Digital procedure of scan methodology. (a), The laser scanner. (b), On-site scanning process. (c), The generated scanning models. (d), The extracted key sections. (e), The battery module for digitalizing key sections in Grasshopper. (f), Digital rebuilt accurate models of wall specimens.

than others. This resulted from the construction processes. Owing to the solid connection requirement between the walls and base beams, the inner holes of the 3D printed walls were cast with concrete several hours after printing, which caused obvious deformation of the concrete mold and inflation of the walls in the gravity effect of the inner concrete. Although the irregularity at the bottom of walls existed, the absolute deviations were still significantly smaller than the thickness of walls, as shown in Fig. 5d. Thus, the potential effect of the irregularity on the walls' seismic performance can be neglected. For the convenience, the wall parts at heights between 300 mm and 1200 mm were extracted for further analysis.

Wall specimens PW1 and PW2 were analyzed in detail and evaluated as an illustration. Ten evenly distributed sliced key sections of each wall were extracted. The typical section results are available in Fig. 5a. The periodic outside surface could be observed here. Based on the key sections, the multi-index evaluation system with six normalized deviations was calculated in Fig. 6b. More detailed data on the inclination angle of surfaces, the thickness of a single concrete filament, the wall thickness, and the cross-sectional area could be found in Fig. 5c.

The inclination angle of the surfaces was defined as the angle between the fitted line of the contour and the horizontal X-axis. From Fig. 5c, the surface inclination angles of PW1 and PW2 were

approximately 90° . The variances were within 1° , which indicated that the wall surfaces were basically vertical. The actual printing surfaces were consistent with the original design, which indicated the good quality of 3D printing.

The thickness of every single concrete filament was calculated according to the vertical distance between neighboring locations of the narrowest width of walls. Fig. 5c also shows the calculated thickness of the single concrete layer at sections PW1 and PW2, which was consistent with the design value of 15 mm. This was because the vertical distance between the printing heads and the concrete layer already printed was fixed at the design value of 15 mm, indicating that the printing concrete had good buildability and would not slump. However, there was obvious fluctuation in the thickness of the single layer with a variance of nearly 2 mm. This illustrated that the extrusion rate of the concrete material was still unstable, which resulted in slight irregularities in the 3D printed concrete filaments. The geometric appearance of the printed concrete structures may have been affected.

The wall thickness was calculated from the horizontal distance between the front and back sides of the wall specimens, and the averages and standard deviations of key sections were also displayed. Fig. 5c shows the statistical value of the wall thickness at ten key sections of the wall specimens. The thicknesses of PW1 and PW2 were both larger than

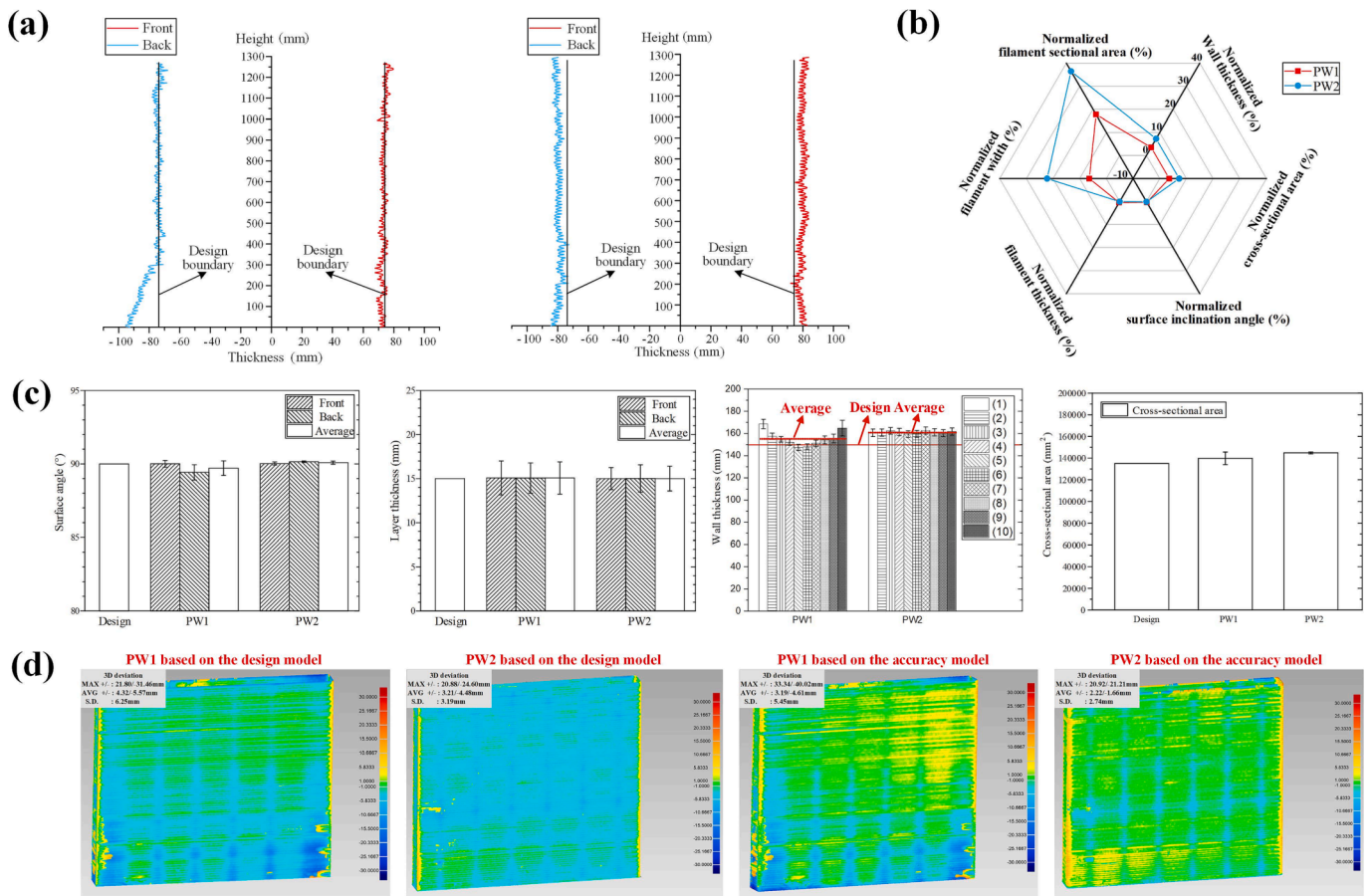


Fig. 5. Geometric analysis and evaluation of 3D concrete printed walls. (a), The 6th key sections of specimens PW1 and PW2. (b), The multi-index evaluation system with six normalized deviation results. (c), Detailed data of inclination angle of surfaces, thickness of single concrete filament, wall thickness, and cross-sectional area. (d), The color maps showing the 3D geometric deviations of PW1 and PW2 based on the design models and accurate models separately.

the designed wall thickness. This behavior resulted from a conservative design width (30 mm) of the printing path. The practical value was larger than 30 mm. It should be found that the concrete materials on the ends of walls were squeezed, thus leading to a larger wall thickness on the ends than the centers due to the existence of the end columns in the PW1 specimen. After all, the wall thickness of the PW2 specimen was relatively consistent, and the surface quality was better than that of the PW1 specimen. It will be necessary to consider the influence of the different internal printing paths on the quality of 3D printed structures during the design process in the future.

The area enclosed by the outline of the section is the cross-sectional area of the wall specimens. Fig. 5c shows the average and standard deviation of the cross-sectional area based on ten key sections. The cross-sectional area was basically close to the design value, indicating that the overall practice size met the design requirements, and the fluctuation of the cross-sectional areas at different locations was quite small.

Macroscopic geometric evaluations were also performed based on the digital models. The geometric evaluations were conducted by the software Geomagic Control. Positive deviations indicated that the practical model was located inside the structures, while negative deviations were located outside the structures. The 3D geometric evaluations of PW1 and PW2 with the design models are shown in Fig. 5d. The deviations between the design models and practical models as well as the distributions were calculated. For PW1, the average positive and negative deviations were +4.32 mm and -5.57 mm, respectively. For PW2, the positive and negative deviations were slightly smaller than those for PW1. The average positive and negative deviations were only +3.21 mm and -4.48 mm, respectively. Moreover, the deviation was significantly larger close to the bottom of the wall than at the top, which

indicated that the internal filling of concrete after printing had a large impact on the printing quality, and the printing concrete had slight accumulation of deformation under the gravitational load. Additionally, there was an obvious negative deviation in the position of the printed concrete bracing trusses. The tight connections between the bracing trusses and the contours could be concluded. The presence of end columns also caused geometric deviations in the related wall surfaces.

Furthermore, geometric evaluations with accurate models were conducted to verify the effect of simulating practical 3D printed structures. The color maps based on accurate models are shown in Fig. 5d. The average positive and negative deviations were reduced to +3.19 mm and -4.61 mm for PW1 and +2.22 mm and -1.66 mm for PW2.

In conclusion, the deviations of the concrete filaments did not further accumulate to the overall structural level owing to the presence of holes inside the walls. This revealed that the multihole and truss structures in 3D concrete printed structures could not only reduce the material cost and corresponding carbon emissions but also dilute the small-scale deviations and maintain good printing accuracy, especially at the structure level. After all, the specimens scanned were verified to have excellent geometric accuracy and reliable printing quality. An experimental study of 3D printed concrete walls was further conducted, and the test results and discussion follow.

5. Mechanical performance

5.1. Seismic loading program

The test setup of seismic experiments is shown in Fig. 6. The test wall specimen was fixed to the reaction floor, while a rigid steel beam was

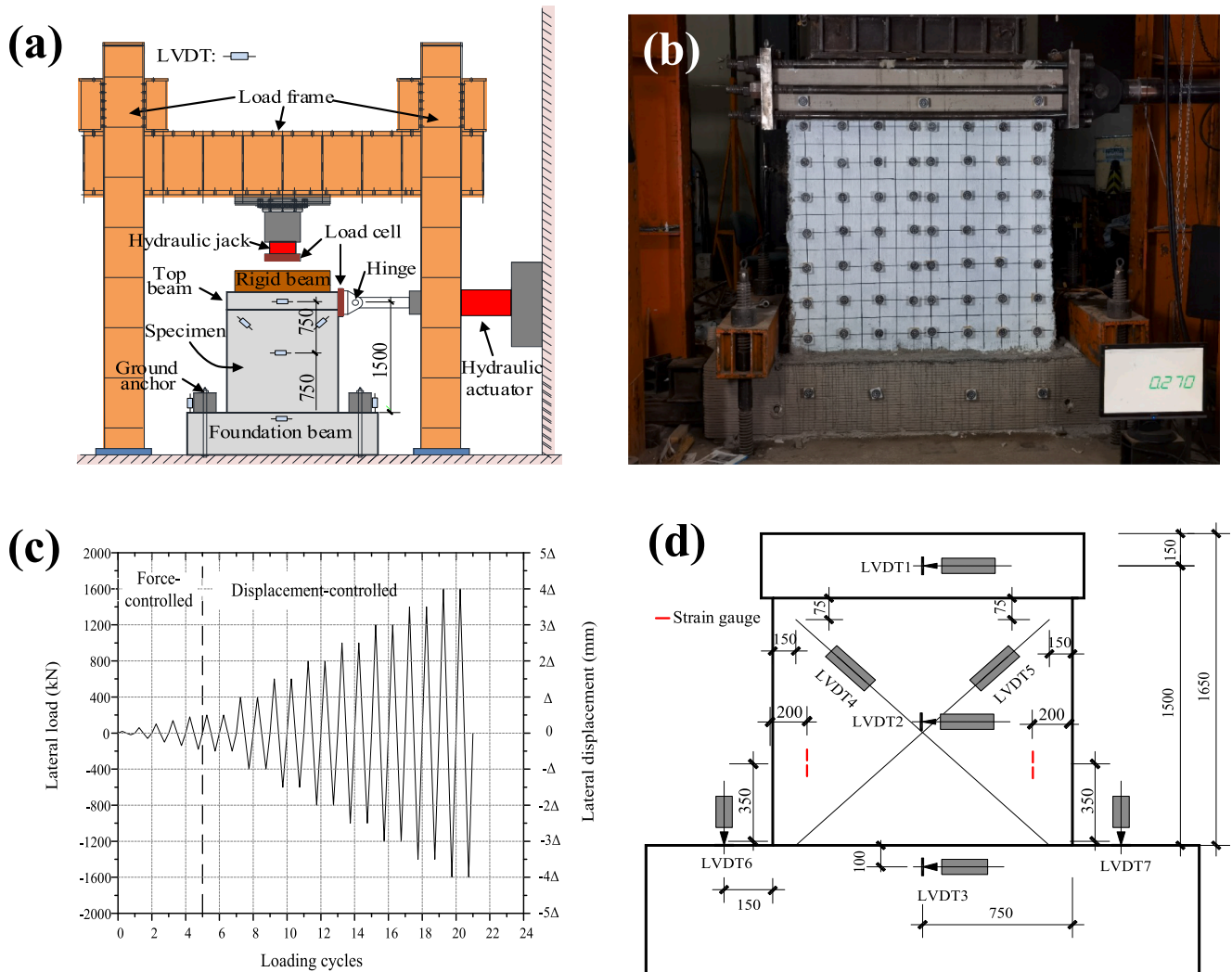


Fig. 6. Test setup and instrumentation (Unit: mm). (a), Schematic illustration of the setup. (b), Loading setup. (c), Loading history. (d), Distributions of displacement and strain gauges.

placed on the top of the wall to uniformly distribute the vertical compressive force. The top beam was clamped to a vertical hydraulic jack and a horizontal hydraulic jack. The constant axial force was applied through the vertical jack, which moved freely in the horizontal direction during tests. Then, the test wall specimen was subjected to formal quasi-static cyclic loading in the lateral direction to simulate the seismic condition. The practical loading setup is shown in Fig. 6b.

Considering the lateral loading history shown in Fig. 6c, the specimens were first loaded to the force-controlled cycle mode with an increment of 40 kN and then underwent displacement-controlled cycles after yielding. Each cycle was repeated twice for all wall specimens. Pull loading was conducted after push loading, defined as positive loading and negative loading, respectively. Preloads of 20 kN for all specimens were applied, ensuring the stability of the loading setup. For better understanding and comparison, the displacement-controlled loading was described by the lateral drift ratio θ , $\theta = \Delta/H$, where Δ is the lateral displacement at the loading point and H is the distance between the horizontal loading point and the wall base. In addition, the specific distributions of linear variable differential transformers (LVDTs) and strain gauges of CFRP textile are illustrated in Fig. 6d. The lateral displacements at different heights and shear displacements were measured. Horizontal and vertical displacements of the bottom beam were also monitored. Moreover, as shown in Fig. 6d, the vertical strain developments of the CFRP textile at 350 mm above the foundation beam

were recorded by strain gauges for all 3D printed wall specimens.

5.2. Seismic performance and failure mode

The mechanical behaviors of the 3DCP wall specimens under quasi-static cyclic loading tests were discussed. Similar to some failure modes of FRP reinforced masonry walls [72–76], specimen PW1 and PW2 showed shear-sliding failure mode characterized by horizontal cracks along the interfaces between layers while specimen PW3 and CW4 showed rocking failure ultimately. Fig. 7 illustrates the failure modes and the crack distributions of all the specimens. The specimen PW1 and PW2 shared a similar failure process. First, the lateral load increased linearly with the applied drift ratio until concrete cracking occurred along with the interfaces between layers at the bottom of the walls. Then, cracks developed as the number of cracks and the crack width increased gradually with continued loading. After the horizontally cracks were bridged, the specimens turn to sliding failure. As for specimen PW3 and CW4, nearly rigid body rotations were observed, centering on the edge toes of walls. Notably, some cracks propagated at an angle of nearly 45° in all specimens, which was a sign of diagonal cracking.

The concrete cracks in 3D printed specimens PW1, PW2 and PW3 were much smaller and denser than those in cast specimen CW4, as shown in Fig. 7. And the reliable bond between 3D printed concrete,

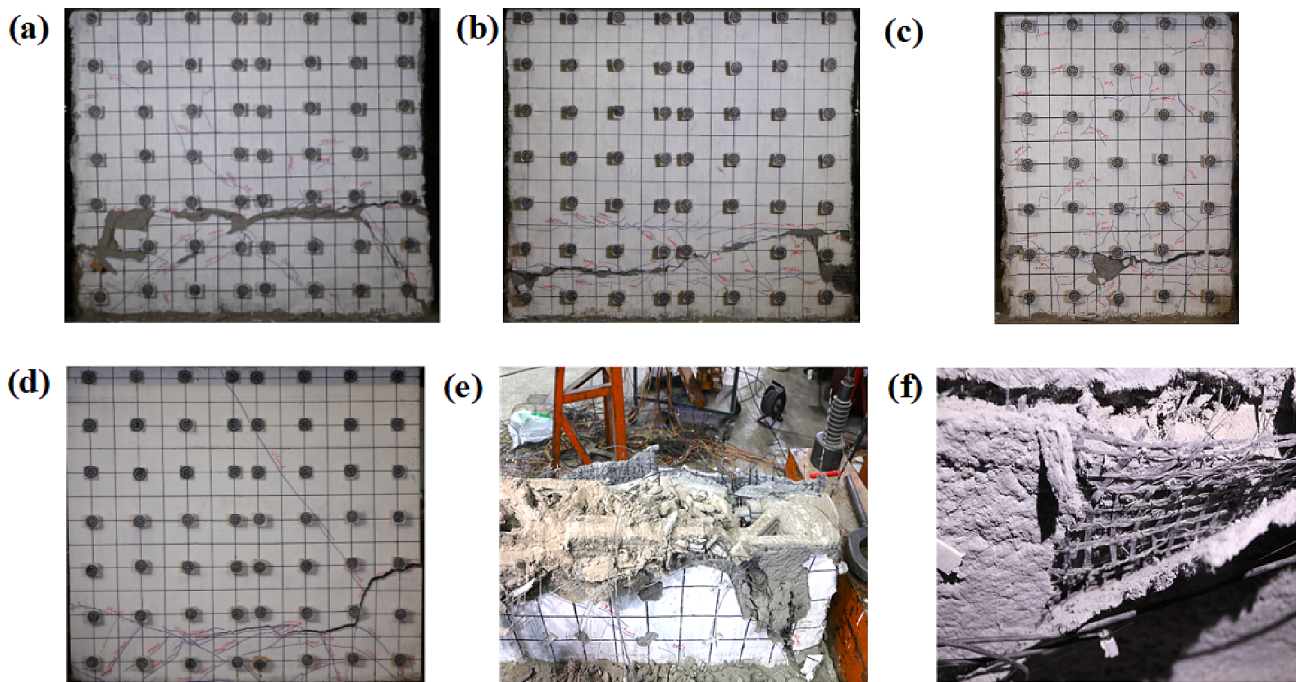


Fig. 7. Ultimate failure modes of the walls. (a), Failure patterns of PW1. (b), Failure patterns of PW2. (c), Failure patterns of PW3. (d), Failure patterns of CW4. (e) The crushed concrete at the wall foot. (f) Failures of CFRP textile.

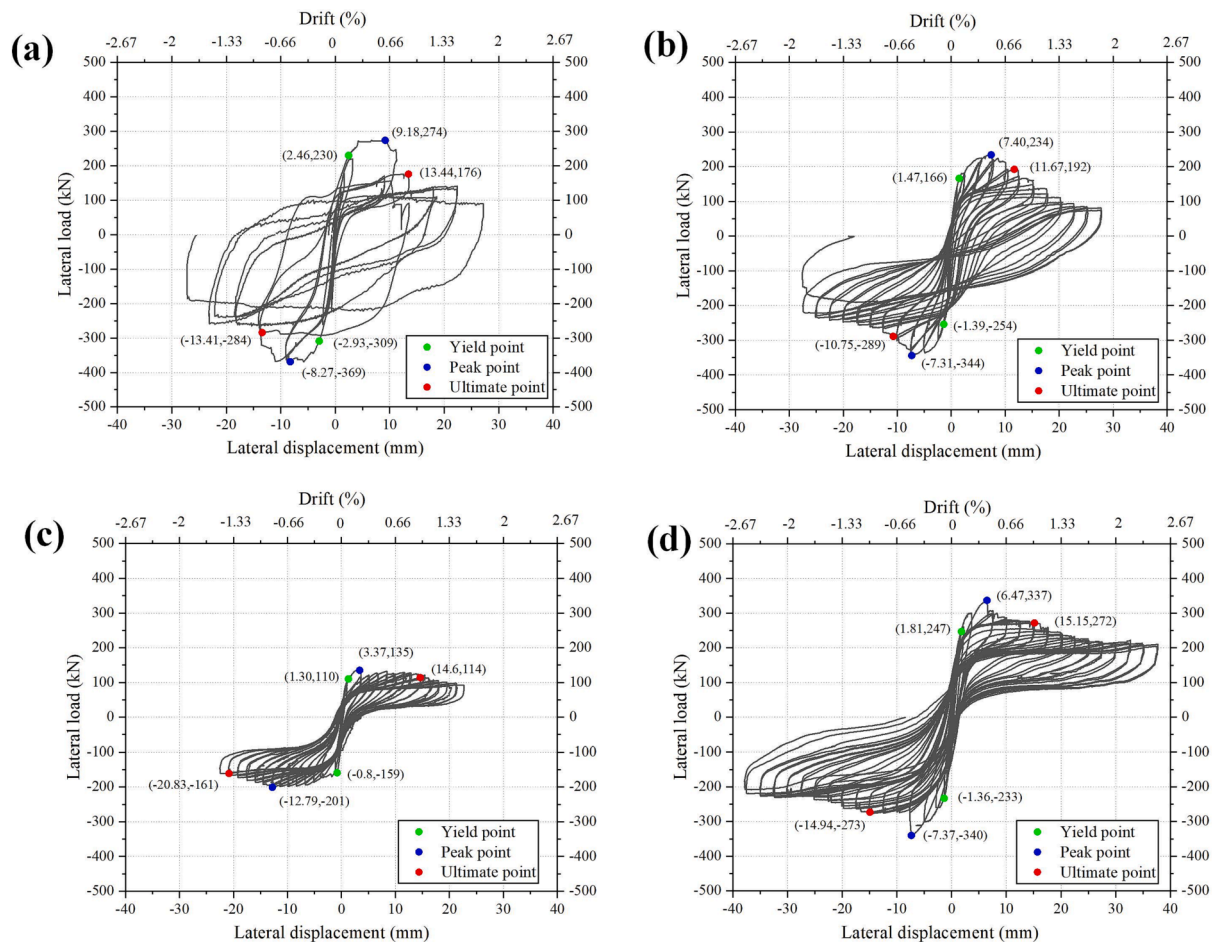


Fig. 8. Lateral load versus lateral displacement response of the walls. (a), PW1. (b), PW2. (c), PW3. (d), CW4.

CFRP textile and ECC layers were verified since no debond, pull-out and fracture were observed before the peak loads of walls, representing that the 3D printed concrete and the reinforcement layers were able to resist the external loading together. After the peak loads, the flexible CFRP textile gradually debonded and ruptured around the concrete cracks (Fig. 7f). In conclusion, the proposed reinforcement method was proven effective in controlling concrete cracks and improving failure modes.

5.3. Hysteretic response

The tested lateral load-lateral displacement hysteretic curves of the wall specimens are illustrated in Fig. 8. The load–displacement curves were characterized by hysteresis loops, which indicated progressive damage of the walls. Compared with the control specimen CW4, the 3D printed concrete wall specimens PW1 and PW2 showed better seismic resistance and behaviors. However, the 3D printed concrete wall specimens showed no better deformation ability. The areas enclosed by the hysteretic hoops of PW1 and PW2 were apparently larger than those of PW3, and the details of the areas enclosed by the hysteretic curves have been discussed in section 5.6.

5.4. Strain development

To determine the effect of the proposed reinforcement method, the vertical strain developments of the CFRP textile are shown in Fig. 9a. The location of strain gauges can be seen in Fig. 6d. Some peak points were not plotted for exceeding the maximum strains of the figures. Owing to the reliable bond between the CFRP textile, ECC layer and 3D printed concrete, the strain of the CFRP textile developed as the loading gradually increased. The strain developments were in the shape of an “L”, with a larger tensile strain and a smaller compressive strain, which illustrated that the CFRP textile played an important role in the tensile strain of structures but was less involved in the compressive strain. Notably, all the strains of the CFRP textile began to obviously increase at the yield loads and then increased rapidly after the peak loads. Then, the CFRP textile reached the ultimate strain before the final failures. This behavior indicated that the CFRP textile took effect mainly after the yield stages with concrete cracking and failed rapidly after the peak points, similar to the reinforcing effect of steel bars in traditional reinforced concrete structures. For specimen PW1, the strain of the CFRP textile at peak loads was 0.54, almost half of the ultimate strain, which indicated the high-efficiency utilization of CFRP. The flexible CFRP textile proved to be efficient in reinforcing and toughening the 3DCP

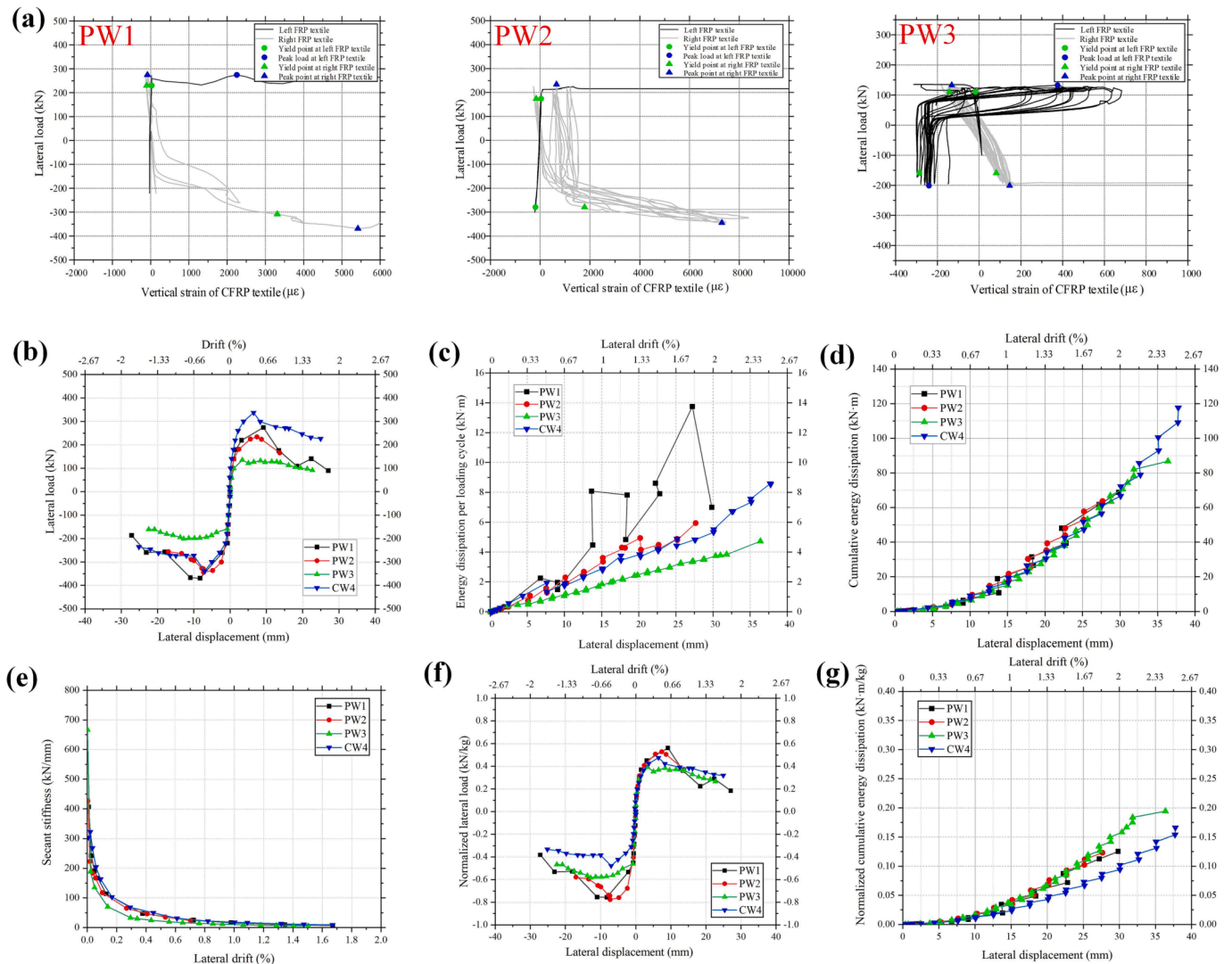


Fig. 9. Key capacities of the walls. (a), The vertical strain development of the CFRP textile in specimens PW1, PW2, and PW3. (b), Envelope curves of the hysteretic response. (c), Energy dissipation per loading cycle. (d), Accumulated energy dissipation. (e), Degradation of secant stiffness. (f), Normalized envelope curves of the hysteretic response. (g), Normalized accumulated energy dissipation.

structures.

5.5. Envelope curve

The envelope curves for the hysteretic response of the walls are presented in Fig. 9b. The skeleton curves of PW1 and PW2 were similar to that of cast specimen CW4. More specifically, the detailed characteristic loads and displacements of the envelope curves were calculated as shown in Table 8. Notably, the ultimate displacement corresponded to the post-peak lateral load, which was 80% of the peak lateral load. Table 8 lists the lateral loads, the lateral displacements, and the displacement ductility at the characteristic points. The displacement ductility coefficient μ_{Δ} is defined as the ratio of the ultimate lateral displacement to the yield lateral displacement.

The yield loads of specimens PW1, PW2, and PW3 were 112.3%, 94.4%, and 49.6% of the yield load of specimen CW4, while the peak loads were 95.0%, 85.4%, and 56.0%, respectively. Because of solid cross-section, the section area of CW4 was far bigger than other 3D printed walls, as shown in Table 2. Without vertical rebars inside, the yield and peak loads of specimen PW1, PW2 and CW4 were controlled mainly by the section area based on the shear-friction theory. Thus specimen CW4 showed higher yield and peak loads than some 3D printed walls. It is noteworthy that specimen PW1 still showed similar mechanical capability with less concrete material compared with specimen CW4 thanks to the FRP reinforcement method and edge columns. Comparing specimen PW1 with other 3D printed specimens PW2 and PW3, further revealed that the increase in the height-width ratio could result in degraded peak load and displacement, and the presence of the edge columns significantly improved the load–displacement response. After all, among the wall specimens, PW1 showed better seismic performances with higher yield load, displacement and peak displacement than PW2, PW3 and CW4.

5.6. Energy dissipation capacity

The dissipated energy is defined by the areas enclosed by the hysteretic curves during the loading cycles. Larger dissipated energy is more beneficial for the seismic resistance of walls. Fig. 9c shows the energy dissipation per loading cycle for the tested wall specimens. And Fig. 9d illustrates the cumulative sum of the dissipated energy of each cycle. The accumulated energy dissipations of PW1 and PW2 were 12.2% and 8.2% greater than that of CW4, respectively, at a displacement of 25 mm, which indicated that the manufacture of 3D concrete printing with a novel reinforcement method could compete with ordinary casting manufacturing. Moreover, the energy dissipation capacity of 3D printed walls was improved by the edge columns and lower height-width ratio. As shown in Fig. 9c, the energy dissipation per loading cycle of specimen PW1 increased over 50% than specimen PW2 after 1% lateral drift. And specimen PW3 have the smallest energy dissipation per loading cycle among wall specimens.

Table 8
Tested characteristic loads and displacements.

Specimen	Loading direction	Yield point		Peak point		Ultimate point			μ_{Δ}
		P_y (kN)	Δ_y (mm)	P_m (kN)	Δ_m (mm)	P_u (kN)	Δ_u (mm)	θ_u	
PW1	Push	230	2.46	274	9.18	176	13.44	0.90%	4.98
	Pull	309	2.93	369	8.27	284	13.41	0.89%	
PW2	Push	174	1.68	234	7.40	192	11.67	0.78%	6.21
	Pull	279	1.93	344	7.31	289	10.75	0.72%	
PW3	Push	110	1.30	135	3.37	114	14.60	0.97%	16.87
	Pull	159	0.80	201	12.79	161	20.83	1.39%	
CW4	Push	247	1.81	337	6.47	272	15.15	1.01%	9.49
	Pull	233	1.36	340	7.37	273	14.94	1.00%	

5.7. Stiffness degradation

The stiffness degradation of the wall specimens was also discussed. The secant stiffness was calculated according to the Chinese standard for seismic tests of buildings [69]. Fig. 9e shows the variation in secant stiffness with lateral drift. There was no observed difference between the PW1, PW2, and CW4 specimens concerning the degraded secant stiffness. The PW3 specimen presented a smaller secant stiffness because of the smaller height-width ratio. For all the specimens, the secant stiffness decreased significantly in the initial stages; then, degradation continued at a slower rate until the secant stiffness was close to 0.

5.8. Normalized capability

Considering the mass of the wall specimens, the normalized mechanical capabilities were also evaluated. Fig. 9f and 9g illustrate the normalized envelope curves and normalized accumulated energy dissipation of the hysteretic responses. As shown in Table 9, characteristic normalized loads and displacements were specifically calculated. The 3D printed concrete walls reinforced by the proposed reinforcement method showed much higher normalized lateral peak load and normalized accumulated dissipated energy compared with the traditional specimen CW4. The results reveal that higher material efficiency and better mechanical properties can be achieved by 3D printing technology with the novel reinforcement method. With proper design and fabrication, 3D printing technology has a promising future in improving material efficiency, reducing carbon emissions, and further replacing traditional construction methods.

6. Conclusions

In this paper, an innovative BEH Loop and corresponding continuous reinforcement method were proposed to automatically construct 3D printed concrete structures. 3D laser scanning technology was implemented in large-scale 3D concrete printed walls, and accurate models were digitally rebuilt. Furthermore, quasi-static cyclic loading tests of the walls were conducted to determine the seismic performance. Based on the results and discussions, the following conclusions can be drawn:

- 1) The concept of the Brain-Eyes-Hands Loop was defined and presented for automatic construction by describing the relationships of design, measurement, and construction processes. As one of the key parts, flexible FRP textile reinforcement offers an effective reinforcing solution for 3D printed concrete structures without electrochemical corrosion problem.
- 2) Through 3D laser scanning technology, the digital rebuilding and geometric evaluation of large-scale 3DCP structures were realized. The accurate models showed great similarity to the real structures, which illustrated the effective eye-to-brain feedback process for the design stage. The specimens tested were verified to have good geometric accuracy and reliable printing quality based on a multi-index evaluation system.

Table 9

Tested characteristic normalized loads and displacements.

Specimen	Loading direction	Yield point		Peak point		Ultimate point		
		P_y^N (kN/kg)	Δ_y (mm)	P_m^N (kN/kg)	Δ_m (mm)	P_u^N (kN/kg)	Δ_u (mm)	θ_u
PW1	Push	0.42	2.46	0.50	9.18	0.32	13.44	0.90%
	Pull	0.56	2.93	0.67	8.27	0.52	13.41	0.89%
PW2	Push	0.34	1.68	0.45	7.40	0.37	11.67	0.78%
	Pull	0.54	1.93	0.66	7.31	0.56	10.75	0.72%
PW3	Push	0.25	1.30	0.30	3.37	0.26	14.60	0.97%
	Pull	0.36	0.80	0.45	12.79	0.36	20.83	1.39%
CW4	Push	0.35	1.81	0.48	6.47	0.38	15.15	1.01%
	Pull	0.33	1.36	0.48	7.37	0.39	14.94	1.00%

- 3) For the seismic performance of all the 3D printed concrete walls, the failure modes were shear-sliding failure for specimen PW1 and PW2, rocking failure for specimen PW3. The initial cracks occurred preferentially in the interfaces between layers before the flexible CFRP textile gradually debonded and ruptured. The interface capability of 3DCP structures was still one of the main control factors of structural failure in complex loading conditions.
- 4) Based on the experimental results of specimen PW1, PW2 and PW3, smaller height-width ratio and presence of solid edge columns of walls could significantly improve the seismic performance of reinforced 3D printed walls. Comparing with PW2, the peak load and peak deformation of PW1 with solid edge columns increased 11.2% and 18.6%, the energy dissipation per loading cycle increased more than 50% after 1% lateral drift. While the peak load and peak deformation of PW3 are only 52.3% and 92.6% of PW1 with smaller height-width ratio. This may inspire further search for design and optimization of 3DCP buildings.

Although these experiments successfully validated the proposed BEH Loop, they were only the first step for automatically constructing large-scale 3D concrete printed buildings in the future. Tighter connections and more thorough relationships among the brain, eyes, and hands will be explored in future research. More advanced technologies and innovative methods are being explored and introduced to enrich the BEH Loop. In particular, more complex mechanical performances of large-scale curved structures will be further studied.

CRedit authorship contribution statement

Daobo Zhang: Methodology, Investigation, Data curation, Writing – review & editing. **Peng Feng:** Conceptualization, Methodology, Supervision, Project administration, Funding acquisition, Writing – review & editing. **Peizhao Zhou:** Investigation, Validation. **Weiguo Xu:** Conceptualization, Project administration. **Guowei Ma:** Validation, Writing – review & editing.

Declaration of Competing Interest

The authors declare that they have no known competing financial interests or personal relationships that could have appeared to influence the work reported in this paper.

Data availability

Data will be made available on request.

Acknowledgements

The writers gratefully acknowledge the partial support of this research by the National Natural Science Foundation of China (No. U2106219), and the Institute of Guo Qiang, Tsinghua University (No. 2021GQG1001). This work has been supported by the New Cornerstone

Science Foundation through the XPLOER PRIZE 2022.

References

- [1] Viktor M, Naidu NV, Frank W, et al. Large-scale digital concrete construction – CONPrint3D concept for on-site, monolithic 3D-printing. *Autom Constr* 2019;107.
- [2] Guowei Ma, Richard B, da Silva L, Ricardo W, et al. Technology readiness: A global snapshot of 3D concrete printing and the frontiers for development. *Cem Concr Res* 2022;156.
- [3] Timothy W, Ena L, Lex R, et al. Digital Concrete: Opportunities and Challenges. *RILEM Technical Letters* 2016:1.
- [4] Peng F, Xinmiao M, Jian-Fei C, et al. Mechanical properties of structures 3D printed with cementitious powders. *Constr Build Mater* 2015;93:486–97.
- [5] Huang Shuyi Xu, Weiguo LY. The impacts of fabrication systems on 3D concrete printing building forms. *Front Architect Res* 2022;11:653–69.
- [6] Behrokh K. Automated construction by contour crafting—related robotics and information technologies. *Autom Constr* 2004;13:5–19.
- [7] Ahmed GH, Askandar NH, Jumaa GB. A review of largescale 3DCP: Material characteristics, mix design, printing process, and reinforcement strategies. *Structures* 2022;43:508–32.
- [8] Mustafa B, Rahul J, Yasser BM, et al. 3D concrete printing for sustainable and economical construction: A comparative study. *Autom Constr* 2022;134.
- [9] Wen Z, Yamei Z, Lei Ma, et al. Influence of printing parameters on 3D printing engineered cementitious composites (3DP-ECC). *Cem Concr Compos* 2022;130.
- [10] Kequan Yu, Wes McGee, Yan NT, et al. 3D-printable engineered cementitious composites (3DP-ECC): Fresh and hardened properties. *Cem Concr Res* 2021;143.
- [11] Lin Alexander, Goel Abhimanyu, Wong De Hui Alwin, et al. Compressive load-dominated concrete structures for customized 3D-printing fabrication. *Automation in Construction*. 2022;141.
- [12] Ana A, Lex R, Timothy W, et al. A 3D concrete printing prefabrication platform for bespoke columns. *Autom Constr* 2021;122.
- [13] Minghao Bi, Phuong T, Lingwei X, et al. Topology optimization for 3D concrete printing with various manufacturing constraints. *Addit Manuf* 2022;57.
- [14] Qian W, Li W, Guowei Ma. Continuous and adaptable printing path based on transfinite mapping for 3D concrete printing. *Autom Constr* 2022;142.
- [15] Wenxin L, Mingyang Li, Tegoeh T. Variable-geometry nozzle for surface quality enhancement in 3D concrete printing. *Addit Manuf* 2021;37.
- [16] Buswell Richard Xu, Jie Daniel DB, et al. Geometric quality assurance for 3D concrete printing and hybrid construction manufacturing using a standardised test part for benchmarking capability. *Cem Concr Res* 2022;156.
- [17] Lingwei X, Guowei Ma, Fang W, et al. Globally continuous hybrid path for extrusion-based additive manufacturing. *Autom Constr* 2022;137.
- [18] Manuel DDJ, Lukumon O, Anuoluwapo A, et al. Robotics and automated systems in construction: Understanding industry-specific challenges for adoption. *J Build Eng* 2019;26.
- [19] Ammar A, Dina H. Energy efficient 3D printed buildings: Material and techniques selection worldwide study. *J Build Eng* 2020;30.
- [20] Konrad G, Aniko K, Hall DM. DFAB HOUSE: implications of a building-scale demonstrator for adoption of digital fabrication in AEC. *Constr Manag Econ* 2021; 39:853–73.
- [21] Flávio C, Pinto DJ, Helena B, et al. Additive manufacturing as an enabling technology for digital construction: A perspective on Construction 4.0. *Autom Constr* 2019;103:251–67.
- [22] de Soto G, Borja A-J, Jens H, et al. Productivity of digital fabrication in construction: Cost and time analysis of a robotically built wall. *Autom Constr* 2018; 92:297–311.
- [23] Tinoco Matheus Pimentel, de Mendonça Érica Martinho, Fernandez Letícia Ikeda Castrillon, et al. Life cycle assessment (LCA) and environmental sustainability of cementitious materials for 3D concrete printing: A systematic literature review. *J Build Eng*. 2022;52.
- [24] Tramontin SM, Maia FI, de Moraes Elisângela G, et al. 3D printed concrete for large-scale buildings: An overview of rheology, printing parameters, chemical admixtures, reinforcements, and economic and environmental prospects. *J Build Eng* 2020;32.
- [25] Mehrab N, Togay O, Aliakbar G. Effect of supplementary cementitious materials on properties of 3D printed conventional and alkali-activated concrete: A review. *Autom Constr* 2022;138.

- [26] Schuldt SJ, Jagoda JA, Hoisington AJ, et al. A systematic review and analysis of the viability of 3D-printed construction in remote environments. *Autom Constr* 2021; 125.
- [27] Li W, Yang Yu, Liang Y, et al. Interfacial bonding properties of 3D printed permanent formwork with the post-casted concrete. *Cem Concr Compos* 2022;128.
- [28] LTD China Construction Second Engineering Bureau. "The world's first in-situ 3D printed two-storey demonstration building" of China Construction Second Engineering Bureau LTD has attracted widespread attention from the society. 2019.
- [29] Severson Brittny. Shanghai-based WinSun 3D Prints 6-Story Apartment Building and an Incredible Home. 2015.
- [30] Cor Apis. The world's largest 3D printed building. 2022.
- [31] Domenico A, Ferdinando A, Costantino M, et al. 3D printing of reinforced concrete elements: Technology and design approach. *Constr Build Mater* 2018;165:218–31.
- [32] Norman H, Kathrin D, Nikolas WA, et al. Structural stay-in-place formwork for robotic in situ fabrication of non-standard concrete structures: A real scale architectural demonstrator. *Autom Constr* 2020;115.
- [33] Sungwoo L, Thanh Le, Webster J, et al. Fabricating construction components using layer manufacturing technology. *Proc Int Conf Glob Innov Constr* 2009;512–20.
- [34] Lukas G, Jaime M-F, Ana A, et al. Structural behaviour of 3D printed concrete beams with various reinforcement strategies. *Eng Struct* 2021;240.
- [35] Bos FP, Ahmed ZY, Jutinov ER, et al. Experimental Exploration of Metal Cable as Reinforcement in 3D Printed Concrete. *Materials (Basel)* 2017;10.
- [36] Li Zhijian, Wang Li, Ma Guowei. Mechanical improvement of continuous steel microcable reinforced geopolymer composites for 3D printing subjected to different loading conditions. *Composites Part B: Engineering*. 2020;187.
- [37] Zhijian Li, Li W, Guowei Ma, et al. Strength and ductility enhancement of 3D printing structure reinforced by embedding continuous micro-cables. *Constr Build Mater* 2020;264.
- [38] Li W, Guowei Ma, Tianhao L, et al. Interlayer reinforcement of 3D printed concrete by the in-process deposition of U-nails. *Cem Concr Res* 2021;148.
- [39] Jingming C, Zhaoliang S, Xiaoyi W, et al. Effect of reinforcement configurations on the flexural behaviors of 3D printed fiber reinforced cementitious composite (FRCC) beams. *J Build Eng* 2022;46.
- [40] Maryam H, Memari AM, Mehrzad Z, et al. Barbed-wire reinforcement for 3D concrete printing. *Autom Constr* 2022;141.
- [41] Taylor M, Jay S. Bond properties of reinforcing bar penetrations in 3D concrete printing. *Autom Constr* 2020;120.
- [42] Taylor M, Jay S. Mesh reinforcing method for 3D Concrete Printing. *Autom Constr* 2020;109.
- [43] Sabrina K, Gabriel F, Wang Bu, et al. A printability index for linking slurry rheology to the geometrical attributes of 3D-printed components. *Cem Concr Compos* 2019; 101:32–43.
- [44] Wolfs RJM, Bos FP, Salet TAM. Early age mechanical behaviour of 3D printed concrete: Numerical modelling and experimental testing. *Cem Concr Res* 2018;106: 103–16.
- [45] Jie Xu, Buswell RA, Peter K, et al. Inspecting manufacturing precision of 3D printed concrete parts based on geometric dimensioning and tolerancing. *Autom Constr* 2020;117.
- [46] Nair Sooraj A. O., Sant Gaurav, Neithalath Narayanan. Mathematical morphology-based point cloud analysis techniques for geometry assessment of 3D printed concrete elements. *Additive Manufacturing*. 2022;49.
- [47] Peng W, Jie H, Yi T, et al. Seismic performance of reinforced concrete columns with an assembled UHPC stay-in-place formwork. *Eng Struct* 2022;272.
- [48] Binrong Zu, Jinlong P, Zhenxin Z, et al. Mechanical properties of engineered cementitious composites beams fabricated by extrusion-based 3D printing. *Eng Struct* 2021;238.
- [49] Xiaoyu H, Jiachuan Y, Mingjian L, et al. Experimental study on large-scale 3D printed concrete walls under axial compression. *Autom Constr* 2022;133.
- [50] Zhang Ying, Wan Zhiming, Wu Lei, et al. Study on mechanical properties of in-situ printed reinforced concrete wall with core column. *International Conference on Optoelectronic Materials and Devices (ICOMD 2021)*2022.
- [51] Totsawat D, Phoosak P, Withit P. Uniaxial load testing of large-scale 3D-printed concrete wall and finite-element model analysis. *Constr Build Mater* 2021;275.
- [52] Zhang Qian Du, Caixia ZP, et al. Research on axial compression performance of 3D printed concrete wall. *Industrial Construction* 2021;51(36–41):94.
- [53] Cai Jianguo Du, Caixia ZP, et al. Research on eccentric compression performance of 3D printed concrete wall. *Industrial Construction* 2021;51:29–35.
- [54] Peng F, Xinmiao M, Hanqing Z. Mechanical behavior of FRP sheets reinforced 3D elements printed with cementitious materials. *Compos Struct* 2015;134:331–42.
- [55] Teng JG, Chen JF, Smith ST, et al. Behaviour and strength of FRP-strengthened RC structures: a state-of-the-art review. *Proc Institut Civ Eng - Struct Build* 2003;156: 51–62.
- [56] Hamilton HR, Dolan CW. Flexural capacity of glass FRP strengthened concrete masonry walls. *J Compos Constr* 2001;5:170–8.
- [57] Baizhao P, Feng L, Yan Z, et al. ECCs/UHPFRCCs with and without FRP reinforcement for structural strengthening/repairing: A state-of-the-art review. *Constr Build Mater* 2022;316.
- [58] Chinnasamy M, Ajithkumar R, Anisha S, et al. Comparative study on the behaviour of textile reinforced concrete slab with engineered cementitious composite slab. *Mater Today: Proc* 2020;33:1175–80.
- [59] Aohan Z, Shan Li, Dengfeng Z, et al. Shear strengthening of RC beams with corrosion-damaged stirrups using FRP grid-reinforced ECC matrix composites. *Compos Struct* 2021;272.
- [60] Yang Xu, Wan-Yang G, Jian-Guo D, et al. Flexural strengthening of RC beams with CFRP grid-reinforced ECC matrix. *Compos Struct* 2018;189:9–26.
- [61] Jingming C, Jinlong P, Xiangming Z. Flexural behavior of basalt FRP reinforced ECC and concrete beams. *Constr Build Mater* 2017;142:423–30.
- [62] Al-Gemeel AN, Yan Z. Experimental investigation of textile reinforced engineered cementitious composite (ECC) for square concrete column confinement. *Constr Build Mater* 2018;174:594–602.
- [63] Nassir A-G, Yan Z. Using textile reinforced engineered cementitious composite for concrete columns confinement. *Compos Struct* 2019;210:695–706.
- [64] Hinzen Marcus, Brameshuber Wolfgang. Improvement of Serviceability and Strength of Textile Reinforced Concrete by using Short Fibres. *Textilbeton – Theorie und Praxis : Tagungsband zum 4 Kolloquium zu Textilbewehrten Tragwerken (CTRS4) und zur 1 Anwendertagung, Dresden, 36 - 562009 - Dresden, 2009 - S 261 - 272*. 2022.
- [65] Ting G, Ahmed AH, Iurie C, et al. Tensile behavior of hybrid fiber reinforced composites made of strain-hardening cement-based composites (SHCC) and carbon textile. *Constr Build Mater* 2020;262.
- [66] Yu-Zhou Z, Wen-Wei W, Mosalam KM, et al. Mechanical behavior of ultra-high toughness cementitious composite strengthened with Fiber Reinforced Polymer grid. *Compos Struct* 2018;184:1–10.
- [67] Deng L, Lei L, Lai S, et al. Experimental Study on the Axial Tensile Properties of FRP Grid-Reinforced ECC Composites. *Materials (Basel)* 2021;14.
- [68] Zhong-Feng Zu, Wen-Wei W, Harries KA, et al. Uniaxial Tensile Stress-Strain Behavior of Carbon-Fiber Grid-Reinforced Engineered Cementitious Composites. *J Compos Constr* 2018;22.
- [69] 50011-2010 GB. Code for seismic design of buildings. 2010.
- [70] Li Hu, Peng F, Hongwei L, et al. Seismic performance of composite shear walls with embedded FCCCs in boundary elements. *Compos Struct* 2021;257.
- [71] Peng F, Zou Yichong Lili Hu, et al. Use of 3D laser scanning on evaluating reduction of initial geometric imperfection of steel column with pre-stressed CFRP. *Eng Struct* 2019;198.
- [72] Tumialan JG, Antonio M, Antonio N, et al. Shear strengthening of masonry walls with FRP composites. *Composites* 2001:3–6.
- [73] Lunn Dillon S, Rizkalla SH. Strengthening of infill masonry walls with FRP materials. *J Compos Constr* 2011;15:206–14.
- [74] Tomislav K, Mislav S, Tvrtko R, et al. Strengthening of masonry walls with FRP or TRM. *Gradjevinar* 2020;72:937–53.
- [75] ElGawady MA, Pierino L, Marc B. Static cyclic response of masonry walls retrofitted with fiber-reinforced polymers. *J Compos Constr* 2007;11:50–61.
- [76] Francesca S. Seismic retrofitting of traditional masonry with pultruded frp profiles. *Appl Sci* 2020;10:2489.